

Article

Improving Low-Frequency Panel Absorbers with Two-Dimensional Acoustic Black Hole

Michael Funk , Mehmet Sait Özer  and M. Ercan Altinsoy 

Chair of Acoustics and Haptics, Technical University Dresden, Helmholtzstrasse 18, 01069 Dresden, Germany; mehmet_sait.oezer@tu-dresden.de (M.S.Ö.); ercan.altinsoy@tu-dresden.de (M.E.A.)

* Correspondence: mail@michaelfunk.eu

Abstract: Many rooms struggle with the absorption of low-frequency sound due to its long wavelengths. The integration of existing solutions into these spaces is often challenging due to their intricate installations and large depths. To address this problem, a new type of resonance absorber has been developed: the Distributed Mode Absorber (DMA). It consists of a thin vibrating front panel and a volume of enclosed air behind it. This straightforward structure can be utilized to create acoustically functional furniture that can be seamlessly incorporated into rooms. This article is devoted to the structural optimization of the DMA front panel, using the Acoustic Black Hole (ABH) effect known within structural dynamics. A numerical model is constructed using a Finite Element Analysis (FEA) and examined numerically. Several geometric parameters of the ABH are studied with regard to their influence on the vibrations of the front panel. Prototypes are developed and manufactured based on these insights. The quality of the numerical model is verified during the subsequent validation. Finally, the sound absorption of the improved DMA is compared with that of the reference DMA.

Keywords: acoustic black hole; finite element modeling; sound absorption; resonance absorber; modal analysis; meta structure; parametric study



Citation: Funk, M.; Özer, M.S.; Altinsoy, M.E. Improving Low-Frequency Panel Absorbers with Two-Dimensional Acoustic Black Hole. *Appl. Sci.* **2024**, *14*, 1338. <https://doi.org/10.3390/app14041338>

Academic Editors: Claudio Guarnaccia and Domenico Rossi

Received: 31 December 2023

Revised: 22 January 2024

Accepted: 2 February 2024

Published: 6 February 2024



Copyright: © 2024 by the authors. Licensee MDPI, Basel, Switzerland. This article is an open access article distributed under the terms and conditions of the Creative Commons Attribution (CC BY) license (<https://creativecommons.org/licenses/by/4.0/>).

1. Introduction

Appropriate room acoustics has increased in importance in daily life. A suitable reverberation time must be ensured for speech intelligibility or the appropriate sound reinforcement of the room. Recommended reverberation times are defined in standards such as DIN 18041 [1]. These reverberation times can be adjusted by treating rooms with various absorbers, e.g., porous or resonant absorbers [2]. In addition, combinations of porous and resonant absorbers can also be used for improving transmission loss for noise suppression [3]. Low-frequency sound poses unique challenges when it comes to noise control and acoustic treatment. Unlike higher frequencies, low-frequency sound waves possess longer wavelengths and greater energy, making them more difficult to effectively absorb and attenuate. This leads, for porous materials, to a requirement for very thick absorbing structures which is not practical for many applications. To overcome this issue, the commonly preferred absorber types for low-frequency sound absorption are resonant absorbers. Specifically, panel absorbers are a possibility to achieve low-frequency absorption, while keeping the installation space low. To work efficiently, panel absorbers usually need to have a significant surface area to achieve low-frequency sound absorption [4]. Its principle is based on using resonant frequencies of the vibrating membrane or panel for dissipating the incident sound energy [5]. For this reason, resonance absorbers are effective at a narrow frequency bandwidth in the vicinity of small numbers of modes (mostly, first mode). To further improve panel absorbers, it's possible to make use of the multimodal structural vibrations a panel shows under pressure excitation. Concepts for this kind of absorber have been studied for several years, such as VPRs (Verbund Platten Resonators) [4]

and DMAs (Distributed Mode Absorbers) [6–9]. It has been shown theoretically [4] and practically [9] that increasing the number of excitable modes leads to an increase in the sound absorption. This study is devoted to the inclusion of Acoustic Black Holes to panel absorbers for improving the low-frequency sound absorption performance.

The Acoustic Black Hole (ABH) is a moderately recent phenomenon to control the vibrational behavior of plates and beams. It is based on the theoretical findings of Mironov [10]. When structure-borne sound is propagating in a flexural wave, a power-law-shaped profile (wedges) improves the damping behaviour significantly. The waves are entering the indentation, and successively slow down due to decreasing material thickness. For an infinitesimally thin material, this ultimately results in a fully absorptive system. However, there always needs to be a truncation in practice. The use of thin damping layers on this wedge has been suggested to increase the effectiveness of ABH designs for damping flexural vibrations [11,12]. It is also possible to extend the power-law profile to generate two-dimensional tapered indentations, which are also referred to as 2D ABH in circular [13,14] or elliptical forms [15]. Coupled systems consisting of ABH embedded panels and air back cavities have recently been studied numerically and experimentally [16–18]. ABH has been successfully applied for vibration and noise reduction in structures [19,20].

ABH can be designed to perform better for selected frequency ranges. Local ABH modes have been found to be dominant in the low-frequency performance of absorption in the structural response [21–23]. Below the first mode of ABH, the structural response has been claimed to be similar to a plate of uniform thickness, and thus, the first mode of ABH is considered to be the cut-on frequency [19,24,25]. At higher frequencies, the effectiveness of ABH increases due to the increase in the modal density and overlaps [21]. In order to tune the cut-on frequency, adjusting the size of the Acoustic Black Hole is the basic design option. The effects of different geometrical parameters and their coupling has been studied for a 1D ABH beam by Shepherd [26] and Hook [23]. Alternatively, tuned mass dampers [27] or active control patches [28,29] can be used for improving the low-frequency behaviour. Du et al. [30] investigated the effects of ABH parameters such as size, orientation, number, residual thickness and damping layer on the sound insulation of circular plates. The experimental and numerical results showed that the circular plate containing a single ABH in the center position can enhance the transmission loss. It has also been claimed that the orientation of the ABH side has a small effect on the sound transmission loss of the studied plate. Liang et al. [31] investigated the mid- and low-frequency performance of plates embedded with an array of ABHs. The energy focalization and sound radiation were investigated using FE models. This resulted in the better energy-gathering performance of the plate with the embedded ABH array compared to the plates embedding a large ABH or a single ABH.

This paper focuses on improving the sound absorption of panels using a single 2D acoustic black hole. It is aimed at enhancing the modal behaviour of a panel absorber to increase the mode density of the absorber and benefit from local ABH modes. This paper is organized as follows: Section 2 contains the details of the investigation case and the numerical modeling procedure including Acoustic Black Hole generation, the meshing details and boundary and loading conditions. The results of the parametric analyses on the position, residual thickness and size of the ABH are given in Section 3. The experimental validations including the vibration and sound absorption measurements are presented in Section 4.

2. Numerical Modeling

2.1. Geometry Definition

A Distributed Mode Absorber (DMA) consists of a vibrating panel and an enclosed air volume behind the panel. In the scope of this study, the panel is modeled without the frame to observe only the vibrating region. It is created as a surface object (2D shell) starting from the origin with the dimensions in the x and y directions. The volume for the back cavity filled with air is created, starting from the panel area extruding from the depth in

the negative z direction. The already existing housings from previous works regarding Distributed Mode Absorbers (DMAs) [7,9] were used. The front panels of the presented prototypes are made from High Pressure Laminate (HPL) material with a thickness of $h_0 = 3$ mm. Therefore, the model dimensions need to match the dimensions of these. The front panel is $L_x = 0.5$ m long and $L_y = 0.4$ m wide. With the same area, the air volume is created with a depth of $h_{BC} = 0.12$ m. The DMA geometry is shown in Figure 1.

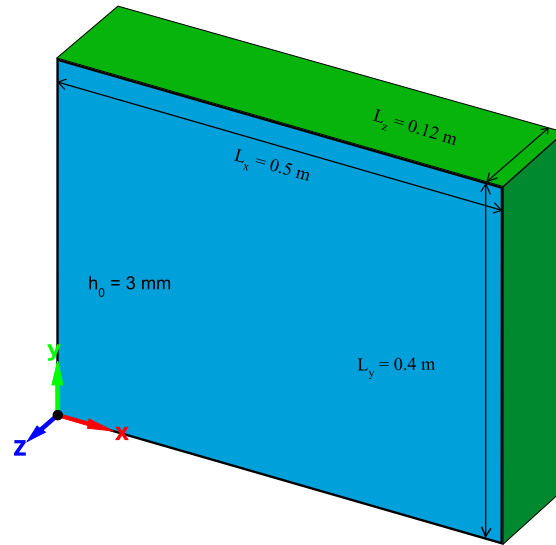


Figure 1. Distributed Mode Absorber (DMA) geometry as it is modeled in the Finite Element Analyses Software. Blue represents the front panel, green represents the back cavity.

2.2. Acoustic Black Hole Geometry

For this work, the 2D Acoustic Black Hole (ABH) approach of Bowyer et al. [13] was used. The typical power-law shape is rotated around its lowest point, creating a circular indentation in the plate. This geometry leads to a set of four variable parameters:

1. \vec{r}_0 —position of the ABH;
2. a —radius of the ABH;
3. m —shape of the ABH;
4. h_{res} —residual thickness of the ABH

The values for the thickness $h(x, y)$ are calculated in Cartesian coordinates with Equations (1)–(3) with radius a , panel thickness h_0 , residual thickness h_{res} , power-law exponent m and the distance from the center of the ABH to the current position $|\vec{r}'|$.

$$h(x, y) = \frac{h_0 - h_{res}}{a^m} \cdot |\vec{r}'|^m + h_{res} \quad \text{for } |\vec{r}'| \leq a \quad (1)$$

$$h(x, y) = h_0 \quad \text{for } |\vec{r}'| \geq a \quad (2)$$

$$|\vec{r}'| = |\vec{r} - \vec{r}_0| \quad \text{with } \vec{r} = \begin{pmatrix} x \\ y \end{pmatrix}, \vec{r}_0 = \begin{pmatrix} x_0 \\ y_0 \end{pmatrix} \quad (3)$$

2.3. Material Properties

The first paper on the ABH effect by Mironov [10] already showed that a maximum reduction in the thickness must be aimed for. Considering this, 3 mm thick High-Pressure Laminate (HPL) is selected as a panel material for the study. It is known from previous studies [6,7] that this thickness without modification has low performance as a DMA front panel. This configuration thickness makes it possible to produce an ABH with a residual thickness $h_{res} = 0.3$ mm using a CNC machine for furniture construction. This corresponds to a factor of $\frac{h_{res}}{h_0} = \frac{1}{10}$, which enables the ABH to significantly influence the

wave propagation on the panel. The material properties used in the numerical modeling are presented in Table 1.

Table 1. Material properties and geometry parameters used in ANSYS for modeling the HPL front plate of the DMA.

Material Property	HPL 3 mm
Young's Modulus E /GPa	10
Poisson's Ratio ν	0.4
Density ρ /kg m ⁻³	1470
Loss Factor ζ /%	2.54

For modeling the air inside the back cavity, the standard material *air* was chosen from the ANSYS library. Its properties are shown in Table 2.

Table 2. Properties of air used for modeling in the FE simulations.

Material Property	Air
Temperature T /K	295.15
Density ρ /kg m ⁻³	1.225
Speed of Sound c /m s ⁻¹	346.250
Viscosity η /kg m ⁻¹ s ⁻¹	1.789×10^{-5}

2.4. Meshing

The numerical modeling of the DMA with the ABH optimized front panel was done with a Finite Element Analysis (FEA) using ANSYS Mechanical. The model was created using a multi-physics approach by combining acoustic and mechanical elements in a single model. For simulating the front panel behavior, quadrilateral 2D shell elements were used. The choice of thickness and panel material influences the flexural wave velocity, which determines the required resolution of the mesh. In the area of the ABH, a finer mesh is required due to the decreasing wavelengths. It is recommended to use at least ten shell elements per flexural wavelength for accurate results [32]. For a residual thickness of the ABH $h_{ABH} = h_0 \cdot \frac{1}{10} = 0.3$ mm, the smallest flexural wavelength λ_{flex} of a plate is computed by Equation (4) from [33], with Young's modulus E , density ρ , Poisson's ratio ν from Table 1 and the upper frequency limit $\omega_u = 2\pi f_u = 2\pi \cdot 500$ Hz of the analysis.

$$\lambda_{flex} = 2\pi \sqrt[4]{\frac{E h_{res}^2}{12\rho\omega_u^2(1-\nu^2)}} \quad (4)$$

The required length for the shell elements is calculated with Equation (5). The resulting shell element length of l_{shell} was rounded so that it is an integer divisor of the panel height L_y .

$$l_{shell} = 8 \text{ mm} \leq \frac{\lambda_{flex}}{10} \approx 9.22 \text{ mm} \quad (5)$$

For simulating the air back cavity, hexagonal 3D elements were used. Acoustic elements are chosen to simulate the stiffness and losses introduced by the enclosed air in the back cavity. It is required to have at least ten elements per wavelength for the chosen acoustic simulation with selected ANSYS element type FLUID220, cf. [32]. The maximum edge length l_{solid} of a solid acoustic element is calculated by Equation (6), with upper frequency limit f_u , its wavelength $\lambda_{f_u} = 0.483$ m and the speed of sound $c = 343$ ms⁻¹.

$$l_{\text{solid}} = 5 \cdot l_{\text{shell}} = 40 \text{ mm} \leq \frac{\lambda_{f_u}}{10} = \frac{c}{10f_u} = 48.3 \text{ mm} \quad (6)$$

A multiple of five times the shell element size was chosen for the fluid element size, to ensure good interaction between the mechanical and acoustical domain. The depth was chosen to fit four elements inside the back cavity. This leads to hexagonal elements with an edge length of $l_{\text{solid},x} = 40 \text{ mm}$, $l_{\text{solid},y} = 40 \text{ mm}$ and $l_{\text{solid},z} = 30 \text{ mm}$.

2.5. Boundary and Loading Conditions

The DMA's resonant panels are attached to a frame that is fixed to a housing with screws. This leads to the assumption of a fixed support boundary condition at all four edges of the panel for the model.

To simplify the computation, the panel is driven by a uniform harmonic pressure of $\hat{p} = 1 \text{ Pa}$ normal to the panel surface. This simplification corresponds to a plane wave that hits the surface vertically with an SPL = 94.5 dB. This condition is e.g., achieved in the far field of a centered mono-pole sound source.

The panel motion is coupled with the air in the back cavity. The numerical coupling between the panel (solid) and the air (fluid) is done using the ANSYS Fluid–Solid Interface. The Fluid–Solid Interface also closes the air volume on the front side. The back cavity (BC) housing is made of 19 mm MDF for the side walls and 30 mm MDF for the rear wall. This prevents the housing from vibrating. They are simulated as a rigid wall, so, a perfect reflection boundary with reflection coefficient $\Gamma = 1$ is used. The modeling approach is depicted in Figure 2.

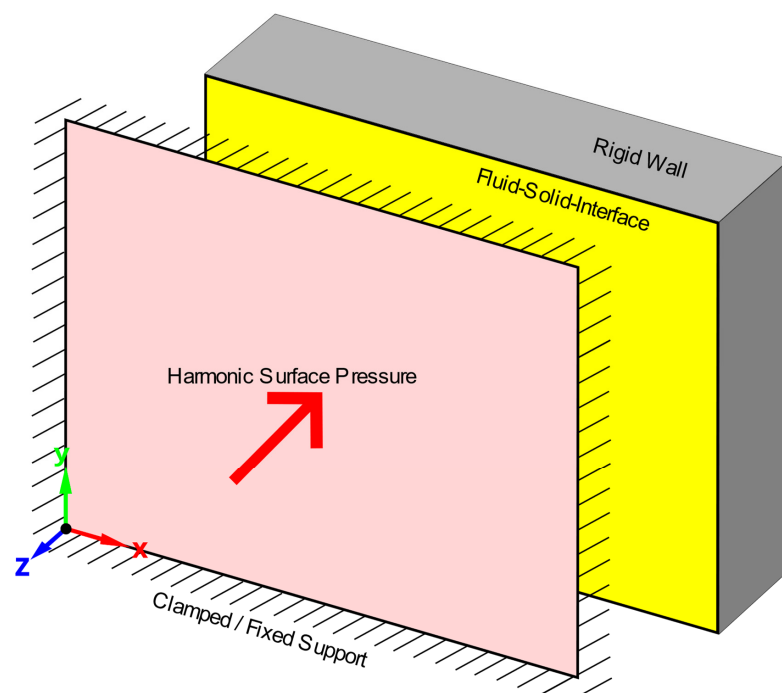


Figure 2. Model details: Red represents the areal loading force in negative z -direction, the black lines represent the clamped/ fixed support boundary condition for the front plate, yellow represents the Fluid–Solid Interface between the two physics regions, grey represents the rigid wall boundary condition for the air volume.

3. Simulation Results

A parametric study on ABH design was performed to show and understand the effect of ABH variations on the panel behaviour. Therefore, different positions, sizes and depths were modeled and analyzed. The results are evaluated and the most promising design option was selected for manufacturing and validating the numerical analysis.

The aim of this study is to improve the diffuse sound absorption α_S of the DMA. The diffuse sound absorption α_S is measured according to the standard DIN EN 20354 [34] inside a reverberant chamber. Due to the statistical nature of this method, various influences e.g., edge diffraction, non-diffuseness and the Sabine formulation can lead to values of $\alpha_S > 1$ [2]. To set a benchmark for the sound absorption results, a target curve is developed in the following. From various studies e.g., [4] it is known that porous and Helmholtz absorbers are sufficient for high-frequency sound absorption. For targeting specific low-frequency absorption, the classical panel absorbers and Helmholtz resonators are an established option. These systems are widely commercially available. The corresponding absorption coefficients are shown in Figure 3 for one example per category. However, broad-band low-frequency absorption is rarely found among commercially available absorbers. The goal of this study is to improve the sound absorption in the gap from $50 \text{ Hz} < f < 250 \text{ Hz}$ between the widely available absorber types. The desired frequency-dependent absorption coefficient is displayed in Figure 3 as the DMA target (passive).

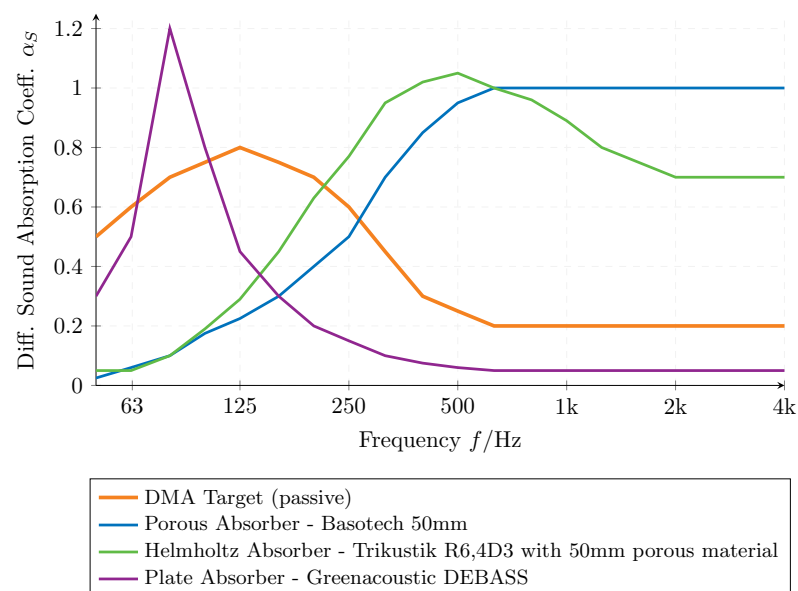


Figure 3. Comparison of the diffuse sound absorption α_S of different absorber types using examples available on the market including DMA target absorption curve.

From the target curve for the sound absorption, some parameters for the mechanical FE simulation of the DMA can be derived. The highest frequency to be analyzed was set to be $f_u = 500 \text{ Hz}$, which determines the FE size of the model. The identification of sound absorption takes place in the logarithmic frequency domain [34]. To save calculation time in the low frequencies, the numerical FE analysis was performed in the linear frequency domain with frequency steps of $\Delta f = 5 \text{ Hz}$. This is possible because the behavior of the DMA panel at low frequencies is determined by the first mode, where no significant change is to be expected due to the ABH.

Mechel [35] showed that the absorption behaviour of a vibrating panel in front of an enclosed air volume is dependent on incident, reflected and scattered sound pressure as well as the spatial distribution of the panel velocity. Therefore, it was decided to evaluate the simulation results via the frequency response of the arithmetic mean velocity $\bar{v}_{x,y}(f)$ for the z-component of the whole vibrating surface. The calculation is done via Equation (7),

where n is the total number of elements on the surface and $|\vec{v}_{z,i}|(f)$ is the amplitude of the element velocity in the z -direction.

$$\bar{v}_{x,y}(f) = \frac{1}{n} \sum_{i=1}^n |\vec{v}_{z,i}|(f) \quad (7)$$

The resulting graphs are evaluated by comparing the $\bar{v}_{x,y}(f)$ of the panels with the embedded ABH to the reference panel. If the mean velocity of the ABH panel exceeds the mean velocity of the reference panel at some frequencies, the sound absorption is expected to be increased at the same frequencies. This way, the target curve shown in Figure 3 defines the frequencies of interest in evaluating the different simulations. Additionally, an equal spacing on the logarithmic frequency axis of the modal peaks is considered best.

The ABH geometry is dependent on four main parameters. Formulas (1)–(3) presented in the previous chapter show the relationships between the parameters. While the panel thickness h_0 is predestined by the material choice for the front plate, the residual height h_{res} , radius a and power-law factor m are free to be chosen by the designer. Additionally, the location of the ABH geometry is varied and analyzed in the following parametric analyses of the mechanical behavior. All the parameters are varied independently to study the influence of each parameter.

Based on the conclusions of Bowyer et al. [13] and Unruh et al. [36], an initial parameter set was chosen to optimize the DMA panel. The selection was made in such a way that the ABH most probable has a significant influence on the structural dynamics of the carrier plate. The parameters, displayed in Table 3, and their effects on the panel are then weighed up.

Table 3. Initial Acoustic Black Hole parameters used in the simulations.

Parameter	Initial ABH
Residual thickness h_{ABH} /mm	0.1
Radius a /m	0.1
Power-law factor m	4

3.1. Position

The ABH effect exerts a significant influence on the flexural wave behavior of its carrier. This is primarily manifested through a reduction in the wave propagation speed c_{flex} in the area of the ABH, which consequently leads to a decrease in the wavelengths λ_{flex} and an increase in the amplitude A_{n_x, n_y} within this area. This leads to a drastic shift in the tensions of the panel, which is expressed through changed mode shapes. Given these impacts, the positioning of the ABH is of great importance and is thus the primary parameter to be analyzed.

The initial ABH presented in Table 3 is moved around in a grid of 3×3 positions with a distance of 10% of the panel dimensions, as shown in Figure 4a. The starting point P11 is the center of the panel, for which the contour of the ABH with a radius $a = 10$ cm is represented in the figure by the dashed circle. The whole circular ABH structure is shifted, with the thinnest point in the center located at the specified position.

The investigations conducted in this section were performed in the absence of the air cavity, so the Modal Superposition Solver was used instead of the Full Method Harmonic Response Solver in ANSYS. This approach facilitated the illustration of mode shapes across all the modes, inclusive of the symmetric even modes, which would have been otherwise suppressed at the ABH positions on the symmetry lines.

A frequency response is considered superior to another if it shows an increase in the normalized mean surface velocity $\frac{\bar{v}_{x,y}}{p}(f)$. In addition, the responses with the most even frequency spacing of the modal peaks on the logarithmic frequency axis are favored.

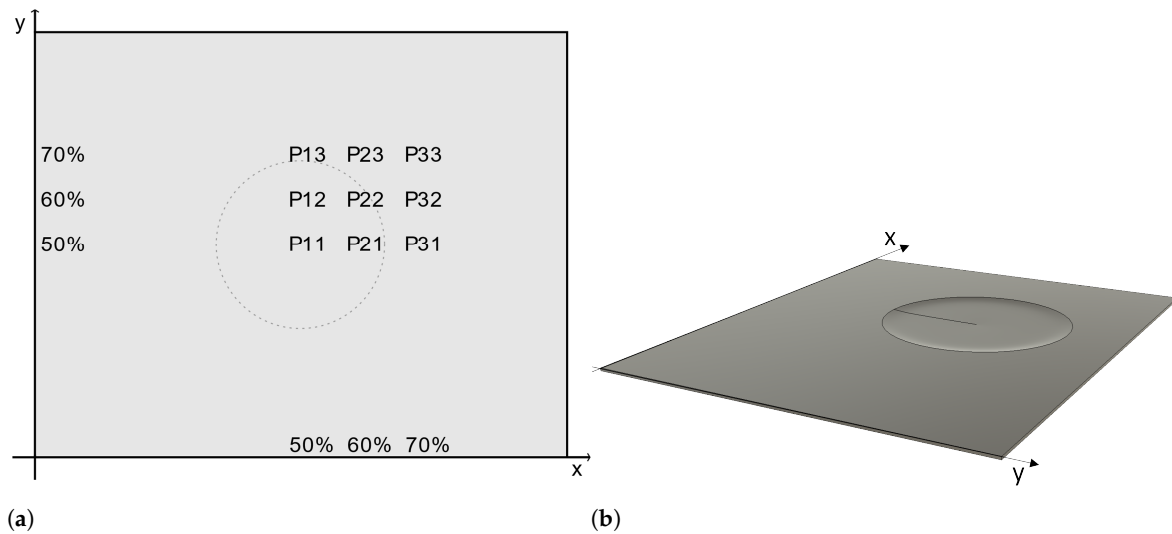


Figure 4. Representations for the position of the ABH: (a) Sketch of 9 different positions for finding the best ABH placement. The dashed circle represents the contour of the ABH for position P11. (b) CAD rendering of ABH with radius $a = 0.13$ m located at position P22.

The evaluation of the simulation outcomes needs to be split into smaller subsets. The partitioning is achieved by assigning the results of the three axes, commencing from the center. The sequence of analysis begins with the x-axis, followed by the y-axis, and finally, the diagonal axis. The best results of these preliminary analyses are then compared in a further graph.

3.1.1. X-Axis

The normalized mean surface velocity $\bar{v}_{x,y}$ results from placing the ABH centered on the y-axis and moving it to different positions on the x-axis are shown in Figure 5 (P11, P21, P31). The blue dots at the top of the graph represent the first four modal frequencies of the reference panel $f_{1,1} = 84$ Hz, $f_{2,1} = 147$ Hz, $f_{1,2} = 192$ Hz and $f_{3,1} = 250$ Hz. The dashed line represents the normalized mean surface velocity $\bar{v}_{x,y}(f)$ of the reference panel without an ABH. Due to the symmetry of the mode shapes for $f_{2,1}$ and $f_{1,2}$, they do not appear on the frequency response. However, the mode shapes for $f_{1,1}$ and $f_{3,1}$ are unsymmetrical; therefore, they are visible in the plotted frequency response.

It can be seen from the graph that the position of the ABH has much influence on the frequency response of the normalized mean surface velocity $\bar{v}_{x,y}$. In general, the desired effect of increasing the surface velocity $\bar{v}_{x,y}$ is achieved for all three positions. However, there are multiple effects introduced by the ABH. The first to mention is the increase in the frequency of the fundamental mode $f_{1,1} \approx 85$ Hz with a position further away from the center. Because the aim is low-frequency improvement, this effect is not desired. The second peak in $\bar{v}_{x,y}(f)$ of the ABH panels is at the same frequency for all three configurations. This occurs due to a new modal frequency which is introduced by the ABH structure itself. The thin material inside the ABH is vibrating in the first circular mode; this frequency $f_{ABH} \approx 120$ Hz is also known as the cut-on frequency. Therefore, it does not depend on the position and needs to be investigated separately. The changes seen at the second panel mode $f_{2,1} \approx 150$ Hz indicate the ability of the configuration to disturb the symmetry of the panel.

Previous research [9] has found that breaking the panel symmetry can be beneficial for improving the sound absorption. This effect also determines the selection of the best configuration from those shown here. Taking the above arguments into account, position P21 is selected as the best choice of the configurations shown in Figure 5.

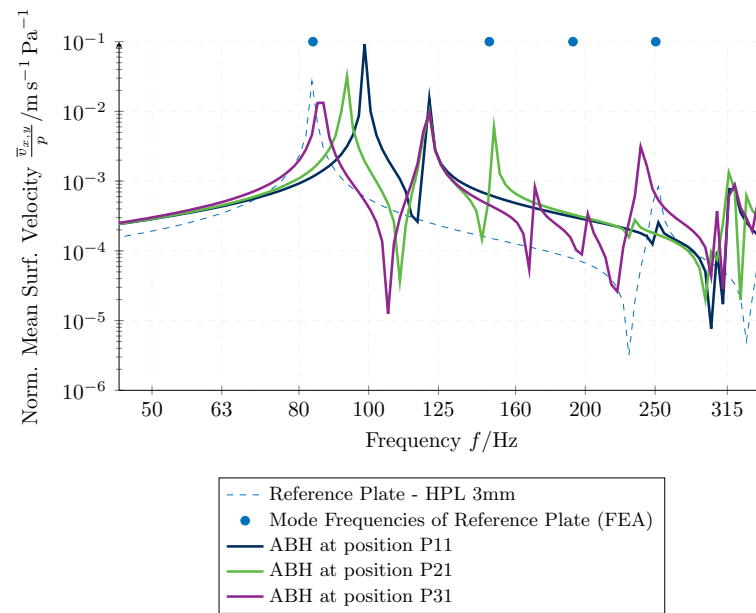


Figure 5. Comparison of the normalised mean surface velocity $\frac{\bar{v}_{x,y}}{p}(f)$ for the x-row of different ABH positions P11, P21, P31.

3.1.2. Y-Axis

For the second subset of positions in Figure 6, the ABH was placed in the center of the x-axis, but moved in the y-direction of the panel (P11, P12, P13). The resonance peaks $f_{1,1} \approx 85$ Hz and $f_{ABH} \approx 120$ Hz exhibit similar effects to those shown in Figure 5. However, due to a change in direction, the excited even mode shifts from the first peak $f_{2,1} \approx 150$ Hz to the second peak $f_{1,2} \approx 190$ Hz. The positioning of the ABH more towards the outer side still results in an increase in the frequency. On the other hand, placing the ABH at the center of the x-axis leads to a decrease in the normalized mean surface velocity $\bar{v}_{x,y}$ at the third panel resonance frequency $f_{3,1} \approx 250$ Hz, regardless of the investigated positions on the y-axis (P11, P12, P13).

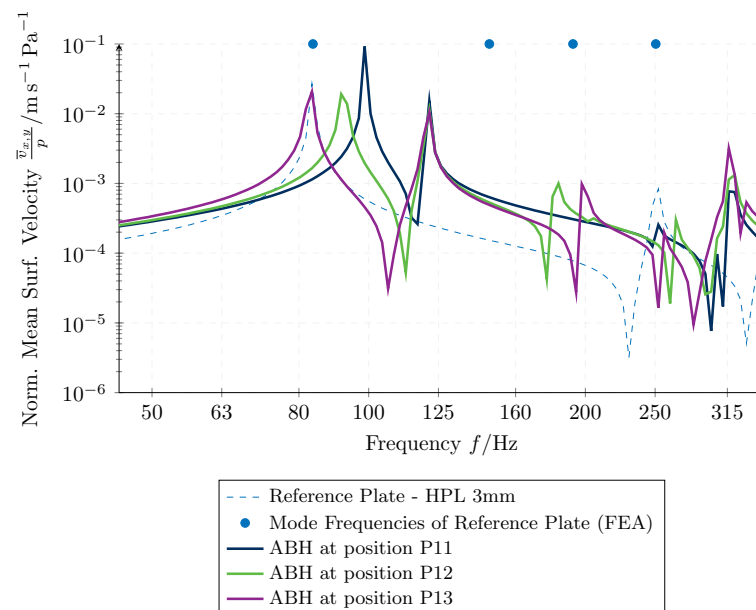


Figure 6. Comparison of the normalized mean surface velocity $\frac{\bar{v}_{x,y}}{p}(f)$ for the y-row of different ABH positions P11, P12, P13.

In respect to the previous descriptions, the response of position P12 proves to be the best in Figure 6. It shows a moderate frequency shift for $f_{1,1} \approx 85$ Hz. For P12, the emphasized even mode $f_{1,2} \approx 190$ Hz appears at a lower frequency compared to P13.

3.1.3. Diagonal Axis

In Figure 7, the ABH was shifted from the center of the panel towards the edge in a diagonal direction (P11, P22, P33).

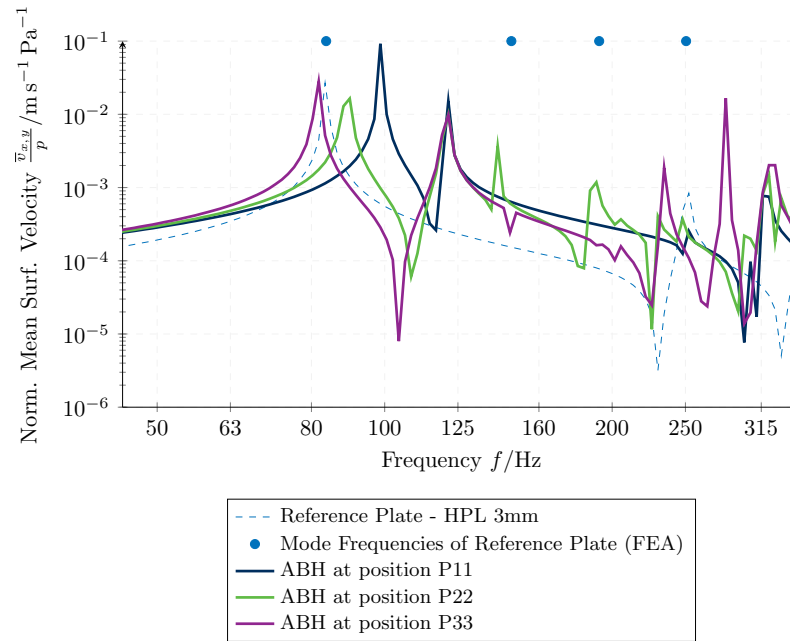


Figure 7. Comparison of the normalized mean surface velocity $\bar{v}_{x,y}/p(f)$ for the diagonal row of different ABH positions P11, P22, P33.

The closer the ABH is positioned to the center, the less the shifting of the fundamental resonance frequency $f_{1,1} \approx 85$ Hz, affirming the same principle as before. The ABH mode also creates a resonant peak in the response at the same frequency $f_{ABH} \approx 120$ Hz as already seen in Figures 5 and 6. At position P22, the frequency response exhibits noticeable peaks at both even modal frequencies, $f_{2,1} \approx 150$ Hz and $f_{1,2} \approx 190$ Hz, as observed with the reference panel modes. This results in a significant improvement in the normalized mean surface velocity $\bar{v}_{x,y}$ between $125 \text{ Hz} < f < 250 \text{ Hz}$ compared to the response at position P11 and P33. On the other hand, placing the ABH at position P33 leads to the suppression of the even modes $f_{2,1} \approx 150$ Hz and $f_{1,2} \approx 190$ Hz. However, it also creates high and narrow peaks above frequencies greater than 250 Hz. It is important to note that these peaks do not align with the objective of this study, which aims to achieve a more evenly distributed arrangement of resonant peaks on the logarithmic frequency axis.

Referring to the descriptions from Figure 7, the best choice is position P22. It enables both even modes $f_{2,1} \approx 150$ Hz and $f_{1,2} \approx 190$ Hz significantly better than the other two positions and in an even frequency distance. The shifting of the fundamental mode $f_{1,1} \approx 85$ Hz is moderate. In addition, P22 incorporates modal peaks for high frequencies $f > 250$ Hz.

3.1.4. Comparison of the Best Positions

Creating more asymmetry by placing the ABH further away from the center does not improve the system’s frequency response in general. It is much more a question of the right placement on the panel than a measure of absolute distances. For this reason, the best three positions, P12, P21 and P22, from the previous graphs, are compared in Figure 8.

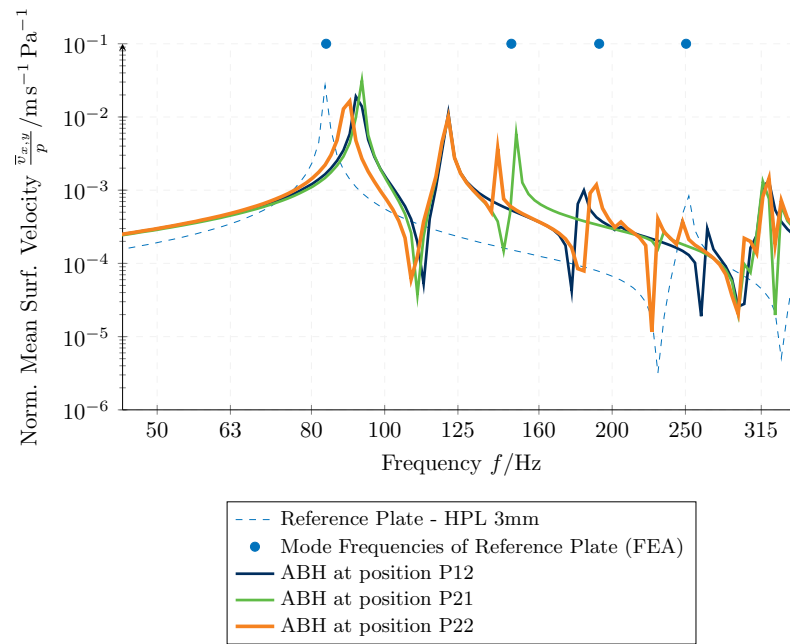


Figure 8. Comparison of the normalized mean surface velocity $\bar{v}_{x,y}^p(f)$ at the three best ABH positions P12, P21, P22.

The most effective normalized mean surface velocity $\bar{v}_{x,y}$ frequency response is observed when the ABH is positioned at P22. At this location, both even modes, $f_{2,1} \approx 150$ Hz and $f_{1,2} \approx 190$ Hz, are excited in a manner similar to the single excitation observed at positions P12 and P21. As a result, the resonance peaks are evenly distributed along the logarithmic frequency axis. Considering the circular ABH mode $f_{ABH} \approx 120$ Hz, the average distance between the peaks below $f < 200$ Hz is approximately one third of an octave. This characteristic enables the DMA to effectively absorb sound in a uniformly spaced manner.

3.1.5. Mode Shapes

The mode shapes of even modes are usually of a symmetric pattern. Because the sum of the velocities cancel out over the whole panel area, these modes do not appear in the frequency response of the normalized mean surface velocity $\bar{v}_{x,y}(f)$. With the asymmetric placement of an ABH, it is possible to activate the lower even modes. The simulations of the mode shapes presented in the following were conducted without the air back cavity by the ANSYS Modal Superposition Solver. In Figure 9, the mode shapes of the first four modes $f_{1,1} = 84$ Hz, $f_{2,1} = 147$ Hz, $f_{1,2} = 192$ Hz and $f_{3,1} = 250$ Hz are shown for the reference panel.

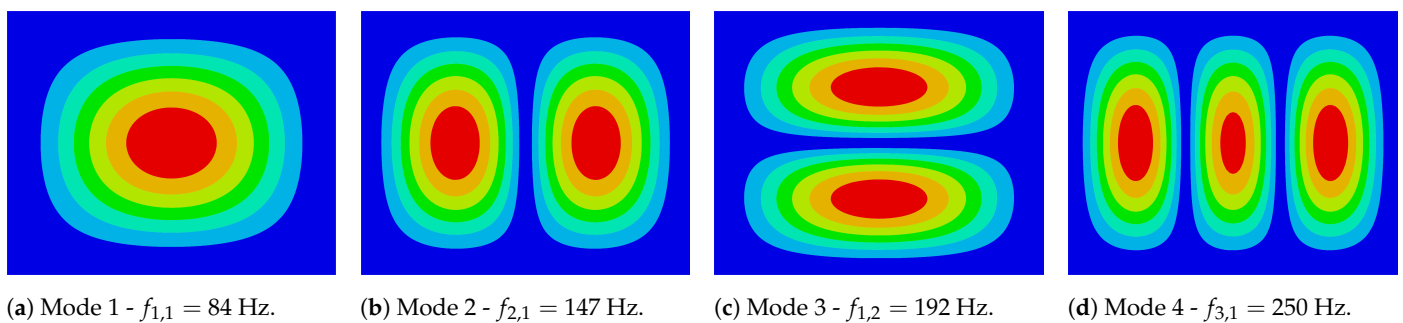


Figure 9. First four mode shapes for the uniform reference panel.

The mode shapes for placing the ABH at the best position P22 are shown in Figure 10. The impact of the Acoustic Black Hole on the panel is recognizable for all four mode shapes. The peak amplitudes are shifted towards the center of the ABH as intended. While the

basic shape for the first two modes is only deformed, the velocity of the third and fourth modes is bundled in the area of the ABH.

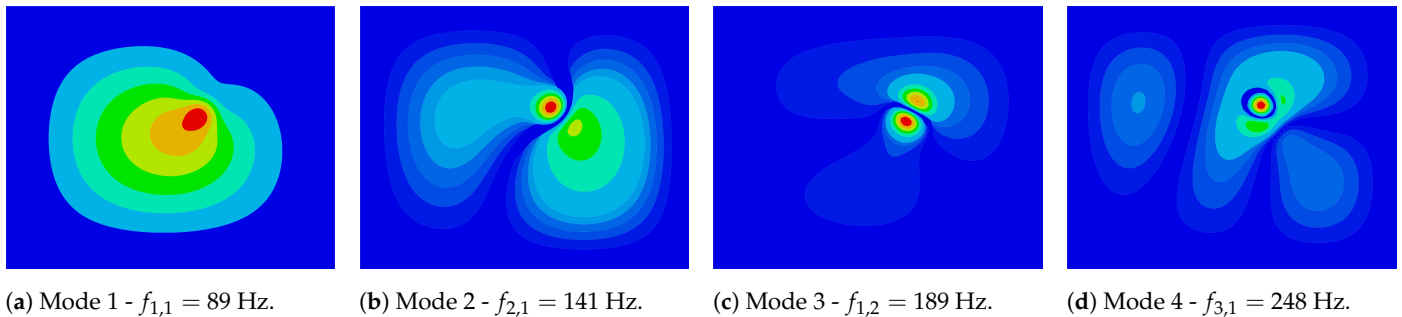


Figure 10. First four mode shapes for the panel ABH ($a = 0.1$ m and $h_{ABH} = 0.1$ mm) at position P22.

3.2. Residual Thickness

The manufacturing process of the two-dimensional Acoustic Black Hole (ABH) geometry on a thin panel with its parabolic shape is a non-trivial task. To achieve an exact result, Computerized Numerical Control (CNC) machining is required. However, even with an accurate machine, an endlessly thin structure is not achievable. Therefore, the thickest but still efficient design must be selected. Figure 11 depicts the normalized mean surface velocity $\bar{v}_{x,y}(f)$ for the same ABH configuration, with radius $a = 0.1$ m and power-law exponent $m = 4$ placed on the center position P11. The residual thickness $h_{ABH} \in \{0.1; 0.3; 0.6\}$ mm is varied to evaluate its effect on the vibration characteristics of the panel. Position P11 was chosen for this analysis to suppress the positive effects of asymmetrical placement shown in the previous Section 3.1.

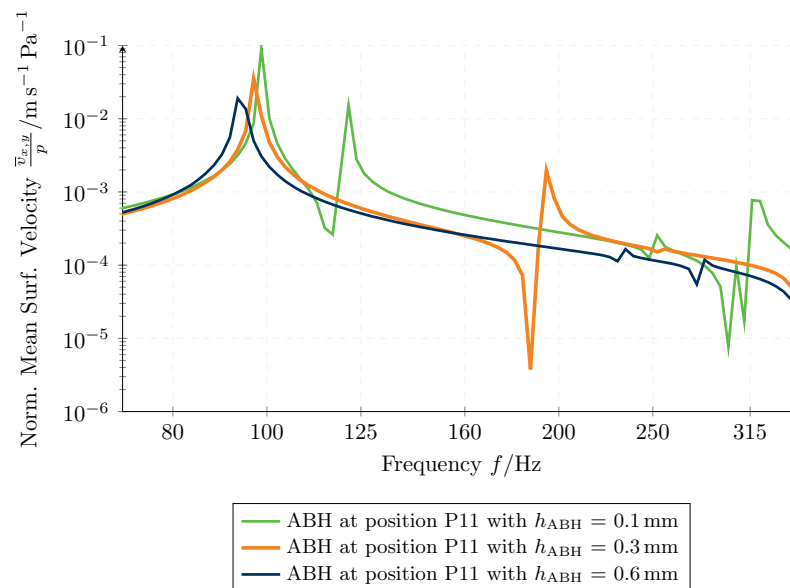


Figure 11. Comparison of the normalized mean surface velocity $\bar{v}_{x,y}(f)$ of three different residual heights at position P11.

The suppression of the even modes results in the outstanding first mode $f_{1,1} \approx 85$ Hz in all three curves, as shown in Figure 11. The resonant peaks for the higher frequencies are therefore attributable to the circular mode f_{ABH} of the ABH. The curve for $h_{ABH} = 0.1$ mm shows a peak at the first mode of the ABH geometry around $f_{ABH,0.1\text{ mm}} \approx 120$ Hz. The curve for $h_{ABH} = 0.3$ mm shows the same ABH mode but at a higher frequency $f_{ABH,0.3\text{ mm}} \approx 195$ Hz. For the curve of the $h_{ABH} = 0.6$ mm, the frequency of the first ABH mode is found at even higher frequencies, hence, it is not visible in the figure. This makes $h_{ABH} = 0.6$ mm not suitable for improving the DMA panel in the target frequency range.

The results of this section indicate that the thinner the structure gets in the middle, the more suitable it becomes in terms of evenly distributed modes within the targeted frequency range. But on the other hand, with a thicker ABH, easier manufacturing and more stability are reached. The practical solution is to select the compromise and move on with a residual thickness of $h_{ABH} = 0.3$ mm.

3.3. Size

The cut-on frequency f_{ABH} of Acoustic Black Holes is essential for its efficiency. For smaller ABH radii, the cut-on frequency increases. For this study, three different-sized ABHs were modeled. For the target frequency range and the used panel properties [37], the cut-on frequency f_{ABH} for a 2D ABH with radius $a < 0.07$ m was shown to not appear in the target frequency range. For three radii $a \in \{0.07; 0.1; 0.13\}$ m, the simulated mean surface velocities $\bar{v}_{x,y}(f)$ are shown in Figure 12.

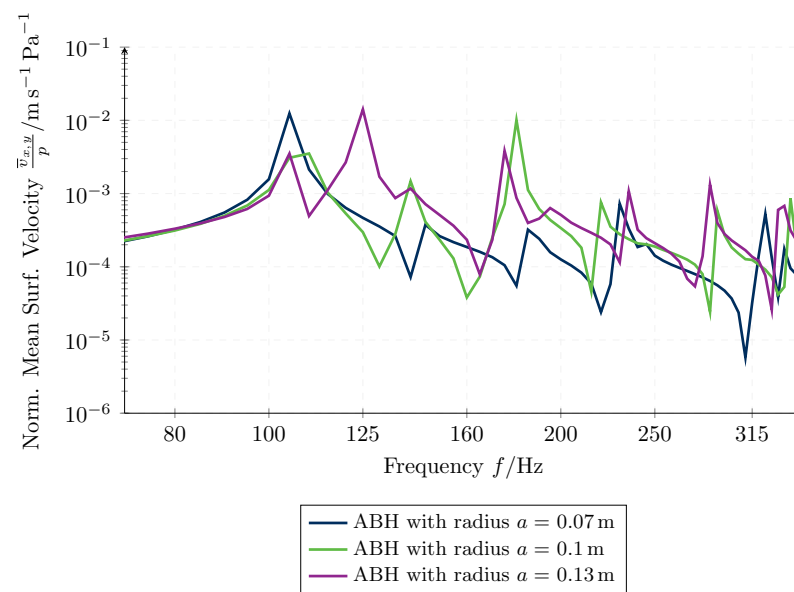


Figure 12. Comparison of the normalized mean surface velocity $\frac{\bar{v}_{x,y}}{p}(f)$ of different sized ABH for three different radii.

The graph shows that the larger the ABH gets, the bigger its impact is. The even modes, which are activated through the unsymmetrical placement of the ABH, indicate this effect quite well. The small ABH with radius $a = 0.07$ m has a quite high cut-on frequency $f_{ABH,a=7\text{cm}} \approx 380$ Hz so the effects seen in Figure 12 are mostly due to breaking the panel symmetry at those frequencies $f_{2,1} \approx 140$ Hz and $f_{1,2} \approx 180$ Hz. On the other hand, the simulations of the two bigger ABHs show a similar normalized mean surface velocity at these modes $f_{2,1} \approx 140$ Hz and $f_{1,2} \approx 180$ Hz, which is significantly higher compared to the smaller ABH. For higher frequencies, the velocity of the $a = 0.13$ m ABH is higher. In addition, the ABH circular mode, responsible for the cut-on frequency $f_{ABH} \approx 125$ Hz, is in between the fundamental mode $f_{1,1} \approx 105$ Hz and the second panel mode $f_{2,1} \approx 140$ Hz. Based on this analysis, it was chosen to manufacture the small ABH with radius $a = 0.07$ m and the big ABH with radius $a = 0.13$ m to verify whether the predictions of the FE model generally hold up in practice.

4. Experimental Validation

The experimental validation process was performed in two sections. First, the vibration responses of the modeled structures were measured in the anechoic chamber. Afterwards, the sound absorption performance of the built structures were measured in standard reverberation room measurements.

4.1. Surface Vibration Measurements

A set of measurements were performed in TU Dresden's Anechoic chamber for the validation of the numerical models. Therefore, a studio monitor (GENELEC 8250A) was located at two meters' distance ($d = 2$ m) from a specimen in the anechoic chamber. It was used in its full frequency range to send acoustic waves to generate oscillations at the panel surface. Rigid frames were built for holding the manufactured front panels. The front panels were interchanged to obtain the effect of the structural characteristics, while the back volume depth was kept as 120 mm. The responses of the front panels were measured with an MMF KS95B.100 mini-accelerometer in four positions, as shown in Figure 13.

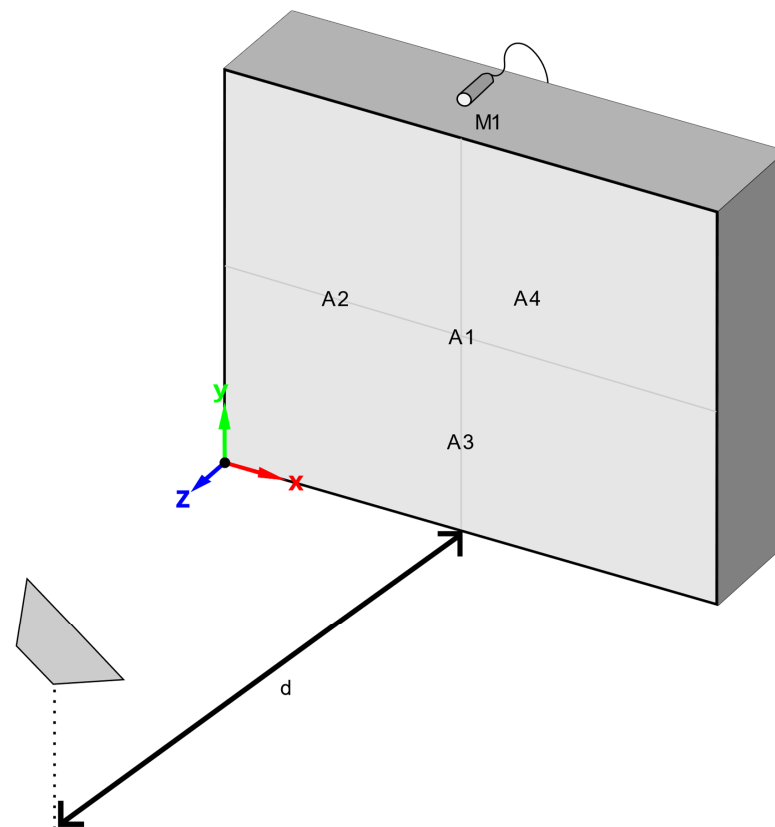


Figure 13. Surface vibration measurement setup.

In order to check the approaching sound pressure on the front surface, a measurement microphone B&K type 4188 was used. The measured vibration response was divided by the approaching sound pressure in order to obtain the response for the unit sound pressure, as in the simulation case. The experimental results are presented in comparison with the simulation results in Figures 14–16 that follow. The simulation results were achieved through multiple fitting iterations of the model. Ultimately, the geometric parameters in the FEM have been set to panel thickness $h_0 = 2.9$ mm and residual thickness $h_{ABH} = 0.35$ mm.

Figures 14–16 show that the predictions of the FEA are in good qualitative agreement with the measurements. While the quality of the quantitative part of the frequency response differs for each measurement position, the prediction of the modal frequencies is sufficient. All of the measurement results show that there is larger damping in the actual structures than the models, since the tip of the frequency peaks are more rounded. The difference in the first frequency for the HPL 3 mm panel was thought to be caused by screwing the front panels tighter, which eventually created a preload on the panel surfaces. Breaking the symmetry effect is noticeable for the designs where the ABH is located off from the center. In general, the prediction quality of the numerical model is more accurate if the selected point is away from the ABH. The differences in the frequency responses can be

caused by topological effects from the manufacturing process that could not be modeled. However, a qualitative description of the acceleration is nevertheless possible for all designs. Furthermore, an agreement of the frequency values can be seen.

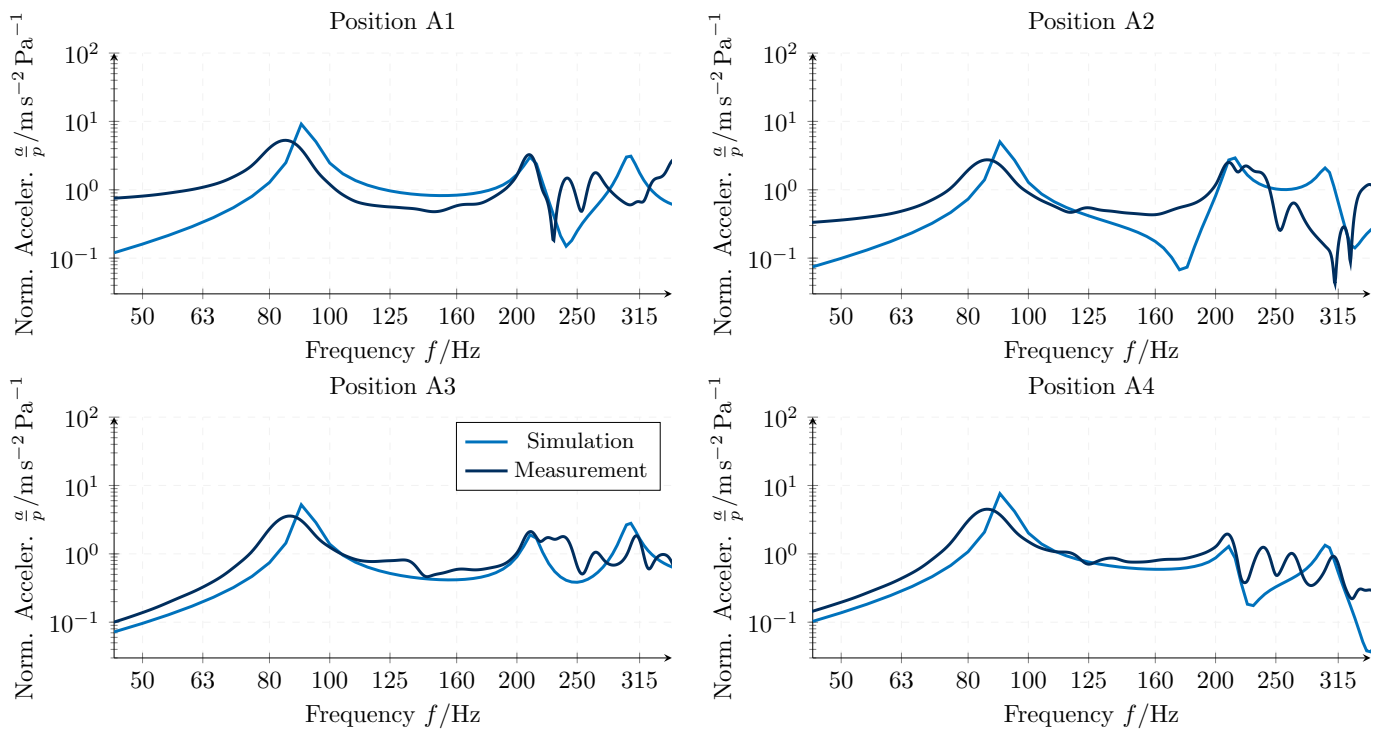


Figure 14. Comparison of the simulated and measured normalised acceleration $\frac{a}{p}$ at 4 points for the reference panel.

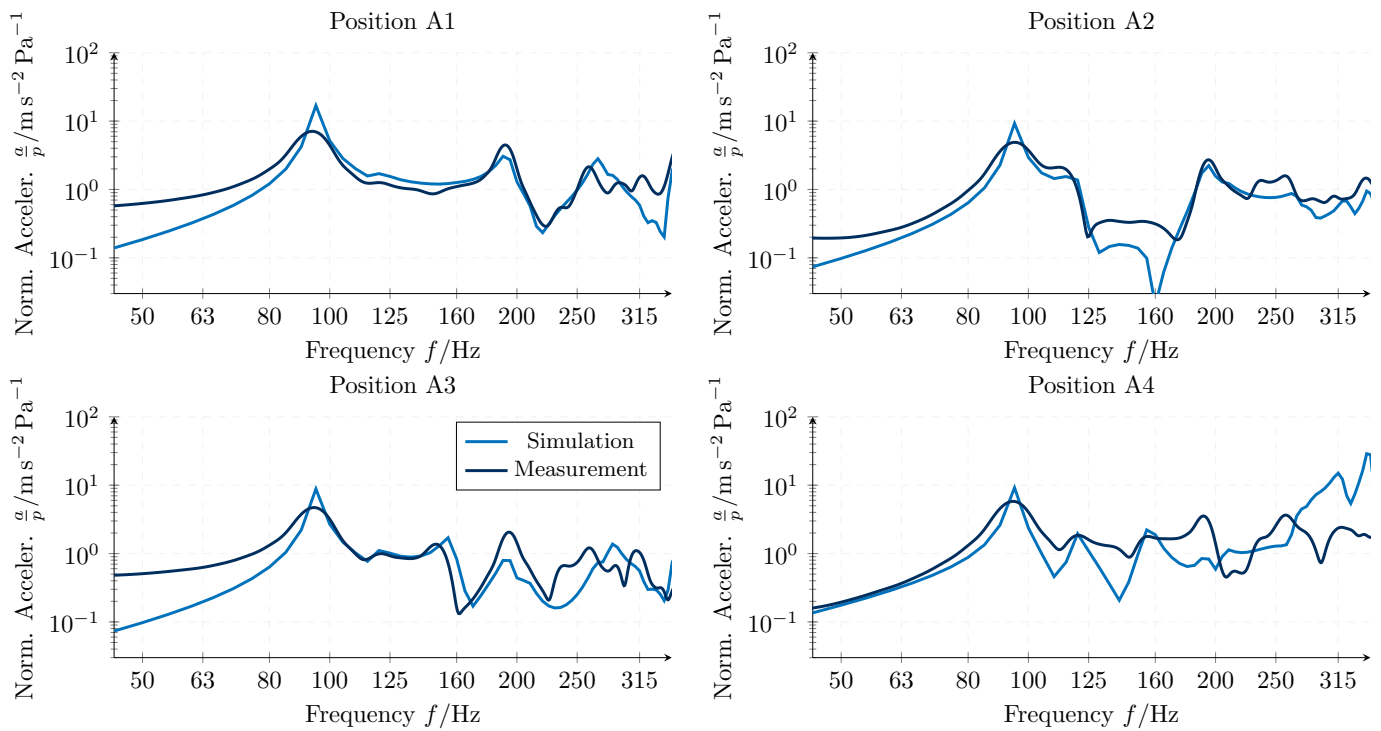


Figure 15. Comparison of the simulated and measured normalised acceleration $\frac{a}{p}$ at 4 points for the panel with ABH of radius $a = 0.07$ m at position P22.

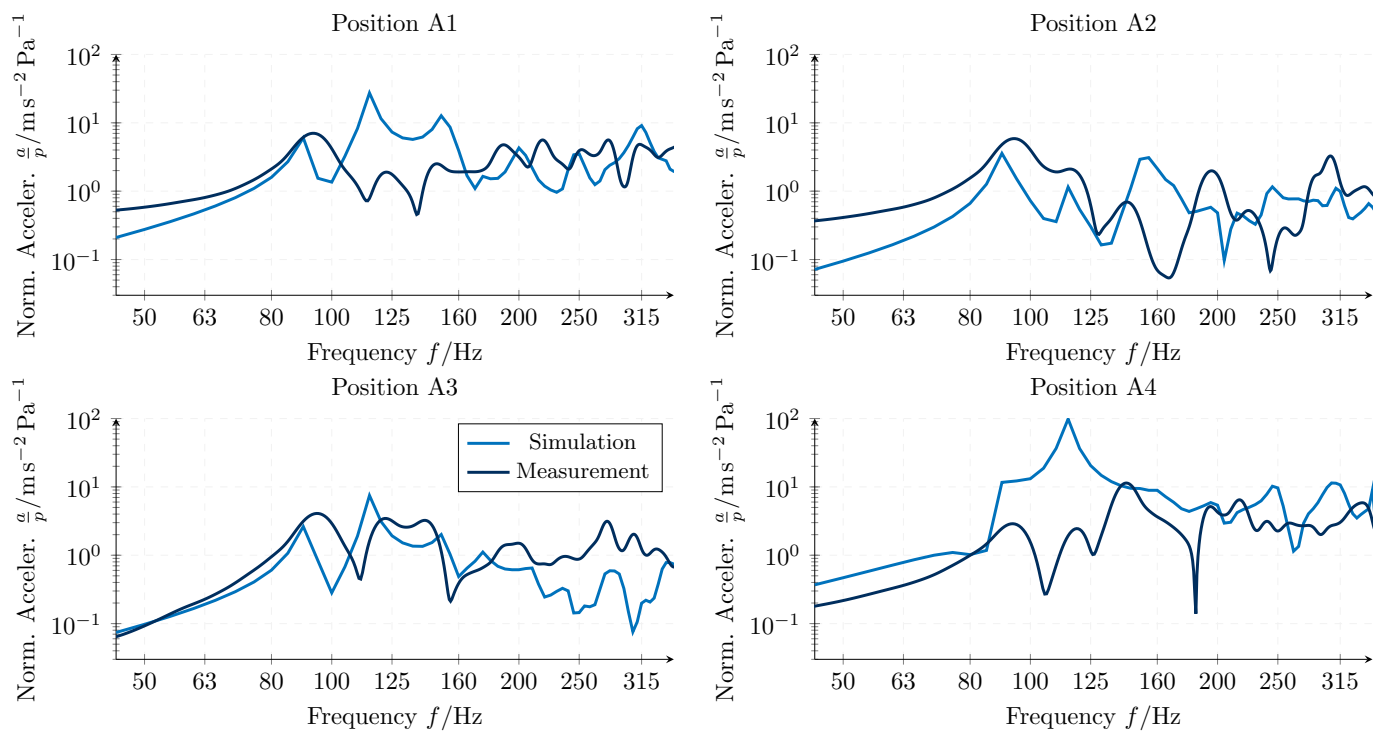


Figure 16. Comparison of the simulated and measured normalised acceleration $\frac{a}{p}$ at 4 points for the panel with ABH of radius $a = 0.13$ m at position P22.

4.2. Sound Absorption Measurements

The sound absorption measurements were performed in a reverberant room that was built according to the ISO 354 standard [34]. The sound absorption performance of uniform HPL 3 mm and a panel with a large ABH (with $a = 0.13$ m at P22) were investigated. Therefore, 42 units for each case were manufactured and measured in the reverberant room (with volume $V = 195 \text{ m}^3$) of TU Dresden, as shown in Figure 17. Three omnidirectional sound sources and six measurement microphones were used during the measurements. The calculated sound absorption are depicted in Figure 18 in 1/24 octave bands.



Figure 17. Measurement setup in the reverberant room.

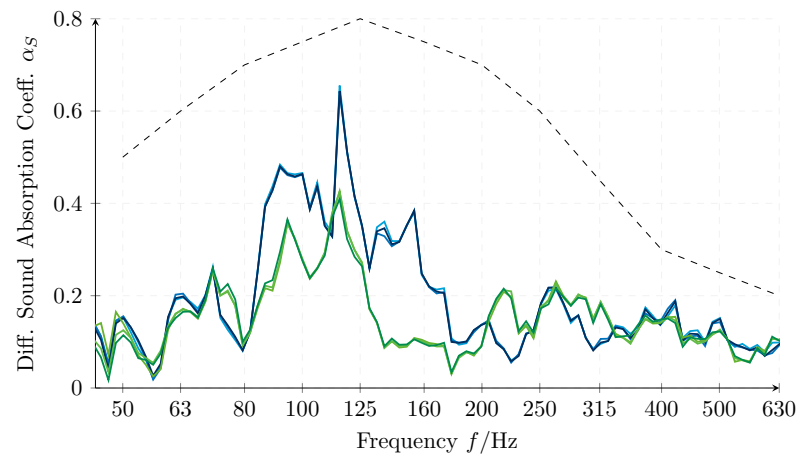


Figure 18. Measured diffuse sound absorption curves of panels. Reference panel measurements (green lines), ABH panel measurements (blue lines) and target curve (dashed line).

It can be seen from the curves that the absorber with the uniform HPL 3 mm panels have absorption peaks at three positions for the selected frequency range. The numerical results have higher vibration amplitudes for those frequency regions as well. However, the levels of absorption are not very high. On the other hand, the effect of including the ABH in the panel can be clearly seen. The sound absorption values are higher than the uniform panel, especially in the 90–170 Hz region, as expected from the numerical simulations.

5. Discussion

The findings of this study reveal that the strategic placement of a two-dimensional Acoustic Black Hole (ABH) off-center on a Distributed Mode Absorber (DMA) front panel enhances its efficacy through several mechanisms.

Primarily, the mode shapes undergo a smooth shift towards the ABH, resulting in the acoustic activation of symmetrical even panel modes. Notably, the first two modes, $f_{2,1}$ and $f_{1,2}$, are of paramount importance in the investigated prototypes. The gradual thickness change within the circular power-law indentation minimizes internal reflections, ensuring a smooth adjustment of modal crest positions. In contrast to an abrupt thickness change [9], the ABH panel achieves a more coherent distribution of flexural waves.

Another advantageous effect contributing to the improved low-frequency absorption is the introduction of a new modal frequency f_{ABH} by the ABH structure. This allows for the creation of a modal frequency situated between the fundamental panel mode $f_{1,1}$ and the second panel mode $f_{2,1}$, representing the most significant inter-modal frequency spacing.

While the study did not explicitly verify the Acoustic Black Hole effect in terms of the internal flexural wave field, the utilization of the ABH shape for the indentation demonstrates substantial potential for enhancing the panel vibration behavior of DMAs at low frequencies. It is noteworthy that the influence of internal flexural wave reflections at the edge of the ABH remains a topic for further investigation in subsequent studies.

6. Conclusions

In this paper, the improvements of the sound absorption performance of panel absorbers including Acoustic Black Holes were numerically and experimentally investigated. A detailed numerical modeling study was performed and the effects of the Acoustic Black Hole position, residual thickness and size were evaluated.

Numerical analyses showed that creating asymmetry on the panels by moving the ABH further away from the center does not lead to a direct improvement in the frequency response of the system. It was seen that the positioning according to a denser mode distribution would improve the panel behavior. For the evaluated case, putting the center of the ABH into the panels at 60%, this position leads to the best design for frequency distribution. The thinner residual thickness was found to be better in the numerical

analysis. However, it was not possible to carve panels down to this thickness; therefore, the experimental studies were conducted with designs with a 0.3 mm residual thickness. Considering the size of the ABH, it can be summarized that the larger the ABH gets, the bigger its impact is.

The experimental studies showed that the presented numerical approach is accurate for determining the vibro-acoustic behavior of panel absorbers incorporating a single ABH indentation. The sound absorption measurements reveal that it is possible to improve the low-frequency sound absorption performance of the panels by including an ABH structure. The sound absorption levels and the number of absorption peaks have been increased with a proper ABH design.

The integration of ABH structures into panel absorbers is a promising concept for advancing their low-frequency sound absorption capabilities. The systematic investigation of ABH design parameters together with their experimental validation contributes to the ongoing pursuit of compact low frequency absorbers. It should be also noted that the performance for the selected case was not superior, since it was known that a thinner uniform panel would have been a better choice. It is therefore necessary to carry out further studies that push the ABH concept to the limits of production facilities.

Author Contributions: Conceptualization, M.F. and M.S.Ö.; methodology, M.F.; software, M.F.; validation, M.F. and M.S.Ö.; investigation, M.F.; resources, M.F. and M.E.A.; data curation, M.F.; writing—original draft preparation, M.F. and M.S.Ö.; writing—review and editing, M.F., M.S.Ö. and M.E.A.; visualization, M.F.; supervision, M.E.A. All authors have read and agreed to the published version of the manuscript.

Funding: This research received no external funding. The APC was funded by the Open Access Publication Fund of TU Dresden.

Data Availability Statement: The data presented in this study are available on request from the corresponding author. The data are not publicly available due to technical difficulties.

Acknowledgments: The manufacturing of the prototypes was performed by Hommel Küchen & Möbelfabrik GmbH, Reichenbach, and the ABH carving operation was performed by Rabatz Design, André Mirtschink, Bautzen, Germany.

Conflicts of Interest: The authors declare no conflicts of interest.

Abbreviations

The following abbreviations are used in this manuscript:

ABH	Acoustic Black Hole
APC	Article Processing Charge
CNC	Computerized Numerical Control
DMA	Distributed Mode Absorber
FEA	Finite Element Analysis
HPL	High-Pressure Laminate
MDF	Medium-Density Fibreboard
VPR	Verbundplattenresonator, german for Composite Panel Resonator
BC	Back Cavity

References

1. *DIN 18041; Hörsamkeit in Räumen—Anforderungen, Empfehlungen und Hinweise für die Planung*. Beuth Verlag GmbH: Berlin, Germany, 2016. [\[CrossRef\]](#)
2. Cox, T.; D’Antonio, P. *Acoustic Absorbers and Diffusers: Theory, Design and Application*, 3rd ed.; CRC Press: Boca Raton, FL, USA, 2016. [\[CrossRef\]](#)
3. Magliacano, D.; Catapane, G.; Petrone, G.; Verdière, K.; Robin, O. Sound transmission properties of a porous meta-material with periodically embedded Helmholtz resonators. *Mech. Adv. Mater. Struct.* 2023, *in press*. [\[CrossRef\]](#)
4. Fuchs, H.V. *Raum-Akustik und Lärm-Minderung*, 4th ed.; Springer GmbH Deutschland: Berlin/Heidelberg, Germany, 2017; pp. 52–70. [\[CrossRef\]](#)
5. Ford, R.D.; McCormick, M.A. Panel Sound Absorbers. *J. Sound Vib.* 1969, *10*, 411–423. [\[CrossRef\]](#)

6. Beyer, F.; Özer, M.S.; Zenker, B.; Merchel, S.; Altinsoy, E.M. Study on the Effect of Back Cavity and Front Panel Materials on the Sound Absorption of Distributed Mode Absorbers. In Proceedings of the DAGA 2022, Stuttgart, Germany, 24 March 2022. Available online: https://fis.tu-dresden.de/portal/files/10254611/Beyer2022a_Study_on_the_Effect_of_Back_Cavity_and_Front_Panel_Materials_on_the_Sound_Absorption_of_Distributed_Mode_Absorbers.pdf (accessed on 1 February 2024).
7. Özer, M.S.; Beyer, F.; Zenker, B.; Merchel, S.; Altinsoy, E.M. Modelling Vibro-Acoustic Behaviour of Membrane Absorbers. In Proceedings of the DAGA 2022, Stuttgart, Germany, 24 March 2022. Available online: https://fis.tu-dresden.de/portal/files/29118200/DAGA_2022_Modelling.pdf (accessed on 1 February 2024).
8. Özer, M.S.; Beyer, F.; Merchel, S.; Altinsoy, M.E. A Study on Multimodal Behaviour of Plate Absorbers. In Proceedings of the Internoise 2022—51st International Congress and Exposition on Noise Control Engineering, Glasgow, UK, 21–24 August 2022. [[CrossRef](#)]
9. Özer, M.S.; Beyer, F.; Merchel, S.; Altinsoy, E.M. A Study on Multi-Thickness Panels for Distributed Mode Absorbers. In Proceedings of the DAGA 2023, Hamburg, Germany, 8 March 2023. Available online: https://fis.tu-dresden.de/portal/files/29118944/DAGA2023_A_Study_on_Multi_thickness_Panels.pdf (accessed on 1 February 2024).
10. Mironov, M. Propagation of a flexural wave in a plate whose thickness decreases smoothly to zero in a finite interval. *Sov. Phys. Acoust.* **1988**, *34*, 318–319. Available online: https://www.researchgate.net/publication/284775645_Propagation_of_a_flexural_wave_in_a_plate_whose_thickness_decreases_smoothly_to_zero_in_a_finite_interval (accessed on 1 February 2024).
11. Krylov, V.V. New type of vibration dampers utilising the effect of acoustic 'black holes'. *Acta Acust. United Acust.* **2004**, *90*, 830–837. Available online: https://www.researchgate.net/publication/233521336_New_type_of_vibration_dampers_utilising_the_effect_of_acoustic_black_holes (accessed on 1 February 2024).
12. Krylov, V.V.; Winward, R.E.T.B. Experimental investigation of the acoustic black hole effect for flexural waves in tapered plates. *J. Sound Vib.* **2007**, *300*, 43–49. [[CrossRef](#)]
13. Bowyer, E.P.; O'Boy, D.J.; Krylov, V.V.; Gaultier, F. Experimental investigation of damping flexural vibrations using two-dimensional acoustic 'black holes'. In Proceedings of the International Conference on Noise and Vibration Engineering (ISMA 2010), Leuven, Belgium, 20–22 September 2010.
14. Bowyer, E.P.; O'Boy, D.J.; Krylov, V.V.; Gaultier, F. Experimental investigation of damping flexural vibrations in plates containing tapered indentations of power-law profile. *Appl. Acoust.* **2013**, *74*, 553–560. [[CrossRef](#)]
15. Deng, J.; Zheng, L.; Guasch, O. Elliptical acoustic black holes for flexural wave lensing in plates. *Appl. Acoust.* **2021**, *174*, 107744. [[CrossRef](#)]
16. Wang, X.; Ji, H.; Qiu, J.; Cheng, L. Wavenumber domain analyses of vibro-acoustic decoupling and noise attenuation in a plate-cavity system enclosed by an acoustic black hole plate. *J. Acoust. Soc. Am.* **2019**, *146*, 72–84. [[CrossRef](#)]
17. Ji, H.; Wang, X.; Qiu, J.; Cheng, L.; Wu, Y.; Zhang, C. Noise reduction inside a cavity coupled to a flexible plate with embedded 2-D acoustic black holes. *J. Sound Vib.* **2019**, *455*, 324–338. [[CrossRef](#)]
18. Du, X.; Liao, X.; Fu, Q.; Zong, C. Vibro-Acoustic Analysis of Rectangular Plate-Cavity Parallelepiped Coupling System Embedded with 2D Acoustic Black Holes. *Appl. Sci.* **2022**, *12*, 4097. [[CrossRef](#)]
19. Pelat, A.; Gautier, F.; Conlon, S.C.; Semperlotti, F. The acoustic black hole: A review of theory and applications. *J. Sound Vib.* **2020**, *476*, 115316. [[CrossRef](#)]
20. Zhao, C.; Prasad, M.G. Acoustic Black Holes in Structural Design for Vibration and Noise Control. *Acoustics* **2019**, *1*, 220–251. [[CrossRef](#)]
21. Denis, V.; Pelat, A.; Gautier, F.; Elie, B. Modal overlap factor of a beam with an ABH termination. *J. Sound Vib.* **2014**, *333*, 2475–2488. [[CrossRef](#)]
22. Feurtado, P.A.; Conlon, S.C. An experimental investigation of acoustic black hole dynamics at low, mid and high frequencies. *J. Vib. Acoust.* **2016**, *138*, 061002. [[CrossRef](#)]
23. Hook, K.; Cheer, J.; Daley, S. A parametric study of an acoustic black hole on a beam. *J. Acoust. Soc. Am.* **2019**, *145*, 3488–3498. [[CrossRef](#)]
24. Aklouche, O.; Pelat, A.; Maugeais, S.; Gautier, F. Scattering of flexural waves by a pit of quadratic profile inserted in an infinite thin plate. *J. Sound Vib.* **2016**, *375*, 38–52. [[CrossRef](#)]
25. Hook, K.; Daley, S.; Cheer, J. Active control of an acoustic black hole using a feedback strategy. *J. Sound Vib.* **2022**, *528*, 116895. [[CrossRef](#)]
26. Shepherd, M.R.; Feurtado, P.A.; Conlon, S.C. Multi-objective optimization of acoustic black hole vibration absorbers. *J. Acoust. Soc. Am.* **2016**, *140*, EL227–EL230. [[CrossRef](#)] [[PubMed](#)]
27. Xiong, Y.; Smith, E.C.; Conlon, S.C. Transmission loss of plates with embedded multi-scale and tuned acoustic black holes. *J. Acoust. Soc. Am.* **2021**, *150*, 2282–2293. [[CrossRef](#)] [[PubMed](#)]
28. Cheer, J.; Hook, K.; Daley, S. Active feedforward control of flexural waves in an acoustic black hole terminated beam. *Smart Mater. Struct.* **2021**, *30*, 035003. [[CrossRef](#)]
29. Hook, K.; Cheer, J.; Daley, S. Control of vibration in a plate using active acoustic black holes. *Smart Mater. Struct.* **2022**, *31*, 035033. [[CrossRef](#)]
30. Du, X.; Huang, D.; Fu, Q.; Zhang, J. Effects of Acoustic Black Hole Parameters and Damping Layer on Sound Insulation Performance of ABH Circular Plate. *Appl. Sci.* **2019**, *9*, 5366. [[CrossRef](#)]

31. Liang, H.; Liu, X.; Yuan, J.; Bao, Y.; Shan, Y.; He, T. Influence of Acoustic Black Hole Array Embedded in a Plate on Its Energy Propagation and Sound Radiation. *Appl. Sci.* **2022**, *12*, 1325. [[CrossRef](#)]
32. ANSYS, Inc. Analysis Guide. Online. 2022. Available online: <https://www.ansys.com/> (accessed on 1 February 2024).
33. Möser, M. *Körperschall: Physikalische Grundlagen und Technische Anwendungen*, 3rd ed.; Springer: Berlin/Heidelberg, Germany, 2010. [[CrossRef](#)]
34. *DIN EN ISO 354:2003-12*; Acoustics—Measurement of Sound Absorption in a Reverberation Room (ISO 354:2003). ISO: Geneva, Switzerland, 2003. [[CrossRef](#)]
35. Mechel, F.P. Panel Absorber. *J. Sound Vib.* **2001**, *248*, 43–70. [[CrossRef](#)]
36. Unruh, O.; Blech, C.; Monner, H.P. Numerical and Experimental Study of Sound Power Reduction Performance of Acoustic Black Holes in Rectangular Plates. *SAE Int. J. Passeng. Cars Mech. Syst.* **2015**, *8*, 956–963. [[CrossRef](#)]
37. Funk, M. Investigating the Acoustic Black Hole Applications for Room Acoustics. Bachelor Thesis, Technische Universität Dresden, Dresden, Germany, 26 June 2023.

Disclaimer/Publisher’s Note: The statements, opinions and data contained in all publications are solely those of the individual author(s) and contributor(s) and not of MDPI and/or the editor(s). MDPI and/or the editor(s) disclaim responsibility for any injury to people or property resulting from any ideas, methods, instructions or products referred to in the content.